

Static stable timelike circular orbits and Aschenbach effect in horizonless solutions of Einstein cubic gravity

Zhen-Hua Zhao^a and Yong-Qiang Wang^b

^a*Department of Applied Physics, Shandong University of Science and Technology, Qingdao 266590, China*

^b*Lanzhou Center for Theoretical Physics, School of Physical Science and Technology, Lanzhou University, Lanzhou 730000, China*

E-mail: zhaozhh78@sdu.edu.cn, yqwang@lzu.edu.cn

ABSTRACT:

In the spacetime of horizonless compact objects described by Einsteinian cubic gravity (ECG), we demonstrate the existence of static stable timelike circular orbits on which massive particles remain at rest relative to distant observers. These static orbits are further identified as the innermost stable circular orbits (ISCOs) in this spacetime. If such static orbits form part of an accretion disk, they would give rise to a ring-like structure that is unaffected by Doppler shifts. Moreover, the Aschenbach effect is shown to be present: the orbital velocity of particles on timelike circular orbits, as measured by a zero angular momentum observer (ZAMO), displays a non-monotonic dependence on the radial coordinate. Additionally, the regions supporting stable circular orbits can be discontinuous, and particles on stable orbits near the center can possess specific energies greater than one ($E > 1$).

Contents

1	Introduction	1
2	Einstein cubic gravity	2
3	Static stable timelike orbits	4
4	Aschenbach effect	8
5	Conclusions and discussions	11
6	Acknowledgment	12

1 Introduction

The detection and characterization of relativistic compact objects, such as black holes and their horizonless alternatives, provide critical tests for general relativity and modified theories of gravity. Since these objects themselves do not emit electromagnetic radiation directly, apart from gravitational-wave detection [1], observing their optical images through surrounding accretion matter offers another crucial approach [2, 3]. This requires a thorough understanding of the motion of accreting particles and photons, as special particle orbits can produce unique observable signatures.

Recently, Collodel, Kleihaus, and Kunz discovered a novel class of orbits around rotating compact objects (e.g., boson stars, hairy black holes, and wormholes) where massive particles remain at rest relative to a distant static observer [4]. These static timelike circular orbits arise from the interplay between the particle's angular momentum and the frame-dragging effect induced by spacetime rotation. Subsequent studies have shown that similar static torus structures may exist around rotating boson stars [5] and scalarized Kerr black holes [6]. Beyond rotating spacetimes, static orbits have also been found in charged, static spherically symmetric black hole solutions [7] and in massive Einstein-Maxwell gravity [8], forming what are termed static spheres.

The existence of static timelike circular orbits implies a characteristic region where the angular velocity of massive particles decreases as the orbital radius decreases, as seen by a distant observer. This behavior is interpreted as the *Aschenbach effect* in static spherically symmetric spacetimes [8–10]. Originally discovered in the context of rapidly rotating Kerr black holes (with spin parameter $a > 0.9953M$), the Aschenbach effect describes a non-monotonic variation in the orbital velocity v^ϕ measured by a ZAMO for test particles on circular orbits [11]. Aschenbach proposed that this non-monotonic velocity profile could excite a distinct 3:1 resonance between radial and vertical epicyclic frequencies,

potentially providing a means to estimate black hole masses [12, 13]. The effect has since been investigated in various contexts, including topology changes of von Zeipel surfaces [14], rapidly rotating Kerr-(A)dS black holes [15], braneworld Kerr black holes [16], charged particles around weakly magnetized rotating black holes [17], and spinning particles in Kerr and Kerr-(A)dS spacetimes [18, 19].

A necessary condition for static timelike circular orbits in static spherically symmetric black hole solutions is that the metric component g_{tt} possesses at least one extremum. This suggests that similar orbits might exist in horizonless solutions where g_{tt} satisfies this condition. Recently, horizonless solutions [20] in ECG [21] have been reported, where g_{tt} typically exhibits extrema, making static orbits possible. Unlike previous models requiring additional matter fields or charges, ECG provides a purely gravitational framework, offering a cleaner setting to study these phenomena.

In this work, we investigate horizonless solutions in ECG and demonstrate the existence of static timelike circular orbits for massive particles in a purely gravitational, electrically neutral, static, and spherically symmetric context. We further identify these orbits as the innermost stable circular orbits (ISCOs) and show that they naturally give rise to the Aschenbach effect.

The paper is organized as follows: Section 2 introduces Einsteinian cubic gravity and its numerical solutions. Section 3 presents the geodesic equations and analyzes the existence and stability of static orbits. Section 4 discusses the Aschenbach effect in these spacetimes. Finally, Section 5 summarizes our results and discusses their implications.

2 Einstein cubic gravity

Einsteinian cubic gravity (ECG) is a higher-order gravitational theory constructed from cubic powers of the Riemann tensor. It has attracted considerable attention due to its unique properties in various aspects. Not only does the theory align with general relativity in its linear perturbation spectrum, ensuring the propagation of massless gravitons without introducing ghost fields, but its cubic curvature term also has dimension-independent coefficients. Notably, ECG is neither trivial nor topological in four-dimensional spacetime, thereby providing a nontrivial effective model for third-order corrections to gravitational theory. Recently, there has been extensive research on ECG models and their extensions. For example, in the context of black holes, studies have covered spherically symmetric solutions [22, 23], generalizations to rotating and charged cases [24–30], and black string solutions [31, 32]. Furthermore, ECG has been extended to research in quasi-topological gravity [33, 34], cosmology [34–37], and wormholes [38–42], demonstrating its broad potential for application across various fields of gravitational physics.

The action of four dimensional ECG is given by [22]:

$$S_G = \frac{1}{16\pi G} \int \sqrt{-g} d^4x (R - G^2 \lambda \mathcal{P}), \quad (2.1)$$

where G is the Newton gravitational constant, R is the Ricci scalar, λ is a dimensionless

gravitational coupling, and

$$\begin{aligned}\mathcal{P} = & 12R_a{}^c{}_b{}^d R_c{}^e{}_d{}^f R_e{}^a{}_f{}^b + R_{ab}{}^{cd} R_{cd}{}^{ef} R_{ef}{}^{ab} \\ & - 12R_{abcg} R^{ac} R^{bd} + 8R_a{}^b R_b{}^c R_c{}^a.\end{aligned}\quad (2.2)$$

For a static spherically symmetric spacetime, we adopt the line element:

$$ds^2 = -f(r)dt^2 + \frac{dr^2}{f(r)} + r^2(d\theta^2 + \sin^2\theta d\phi^2), \quad (2.3)$$

where $f(r)$ satisfies the ordinary differential equation [22]:

$$\begin{aligned}- (f - 1)r - G^2\lambda & \left[4f'^3 + 12\frac{f'^2}{r} - 24f(f - 1)\frac{f'}{r^2} \right. \\ & \left. - 12ff''\left(f' - \frac{2(f - 1)}{r}\right) \right] = \mathcal{C},\end{aligned}\quad (2.4)$$

constant $\mathcal{C} = 2GM$, where M denotes the mass of the object.

Equation (2.4) is highly nonlinear, making it extremely challenging to obtain analytical solution. Therefore, seeking asymptotic solutions near certain points [22, 23] or complete numerical solutions [20] are more practical approaches to analyzing the problem.

It is important to note that although Eq. (2.4) appears as a second-order differential equation, it originates from the third-order field equations of ECG. Specifically, Eq. (2.4) represents a first integral of the original third-order equations, with the integration constant \mathcal{C} . Consequently, three conditions are required to uniquely determine the solution. The spacetime is asymptotically flat, which imposes the conditions:

$$f(\infty) = 1, \quad \text{and} \quad f'(\infty) = 0. \quad (2.5)$$

Here, $f(\infty) = 1$ normalizes the time coordinate at infinity, while $f'(\infty) = 0$ ensures true asymptotic flatness and determines the mass parameter \mathcal{C} through the asymptotic expansion [21] $f(r) \approx 1 - \mathcal{C}/r + \dots$. Additionally, for horizonless solutions, we require regularity at the origin $r = 0$. This provides the third condition:

$$f(0) = f_0 > 0. \quad (2.6)$$

The parameter f_0 characterizes the metric behavior at the center and must be positive to avoid a curvature singularity.

Further, to simplify numerical computations, we introduce the following dimensionless variable substitutions:

$$\frac{r}{GM} \rightarrow r, \quad \frac{\lambda}{G^2 M^4} \rightarrow \lambda, \quad \frac{t}{GM} \rightarrow t, \quad \text{and} \quad \frac{ds}{GM} \rightarrow ds. \quad (2.7)$$

Subsequently, equation (2.4) is simplified by setting

$$G \rightarrow 1, \quad M \rightarrow 1, \quad (2.8)$$

which leaves the redefined λ as the only free parameter.

To ensure the solution covers infinity point, we introduce a compactified coordinate $x = r/(1+r)$ to map the physical domain $r \in [0, \infty)$ onto the computational interval $x \in [0, 1]$. The boundary value problem defined by Eq. (2.4) with conditions (2.5) and (2.6) is then solved using the finite element software FEniCSx [43–45].

For given f_0 and λ , Eq. (2.4) admits two independent branches of solutions, which we label as Branch 1 and Branch 2. Fig. 1 shows example solutions for $f_0 = 0.9, 0.5$, where for a given λ , dashed and solid lines of the same color correspond to the solutions in two branches, respectively. It can be seen from Fig. 1a and 1c that the solutions from the two branches gradually converge as λ decreases.

Within the parameter range considered, not every solution of $f(r)$ possesses a local minimum, though each solution contains at most one. The dependence of the location of this local minimum on the parameter λ is shown in Figs. 1(b) and 1(d). From the figures, we observe that: (1) As λ decreases, the locations of the local minima in the two branches approach each other; (2) For the Branch 1 solution with $f_0 = 0.9$, the location of the local minimum increases monotonically with λ ; for the Branch 1 solution with $f_0 = 0.5$, however, it first increases and then decreases, eventually disappearing when $\lambda \geq 200$; (3) In Branch 2, the location of the local minimum first decreases and then increases as λ grows.

3 Static stable timelike orbits

The action of a unit mass particle moving in this spacetime is given by

$$S = \int g_{\mu\nu} \dot{x}^\mu \dot{x}^\nu d\tau. \quad (3.1)$$

The dot denotes the derivative with respect to proper time τ . To maintain the generality of the formula, we retain the symbolic form of $g_{\mu\nu}$ in the equation and only substitute the specific expression of $g_{\mu\nu}$ into the final result.

Assuming the particle moves in the equatorial plane with $\theta = \pi/2$, the equations of motion are

$$\ddot{r} = \frac{1}{2g_{rr}} \left(g_{tt,r} \dot{t}^2 - g_{rr,r} \dot{r}^2 + g_{\phi\phi,r} \dot{\phi}^2 \right), \quad (3.2)$$

$$\dot{t} = -\frac{E}{g_{tt}}, \quad \dot{\phi} = \frac{L}{g_{\phi\phi}}, \quad (3.3)$$

where the subscript “,r” denotes the derivative with respect to the radial coordinate r . The conserved quantities E and L represent the energy and angular momentum per unit mass of the particle (specific energy and specific angular momentum), respectively.

Additionally, the particle’s motion satisfies the normalization condition:

$$g_{\mu\nu} \dot{x}^\mu \dot{x}^\nu = -1, \quad (3.4)$$

which can be reduced to

$$\frac{1}{2} \dot{r}^2 + V(r) = 0, \quad (3.5)$$

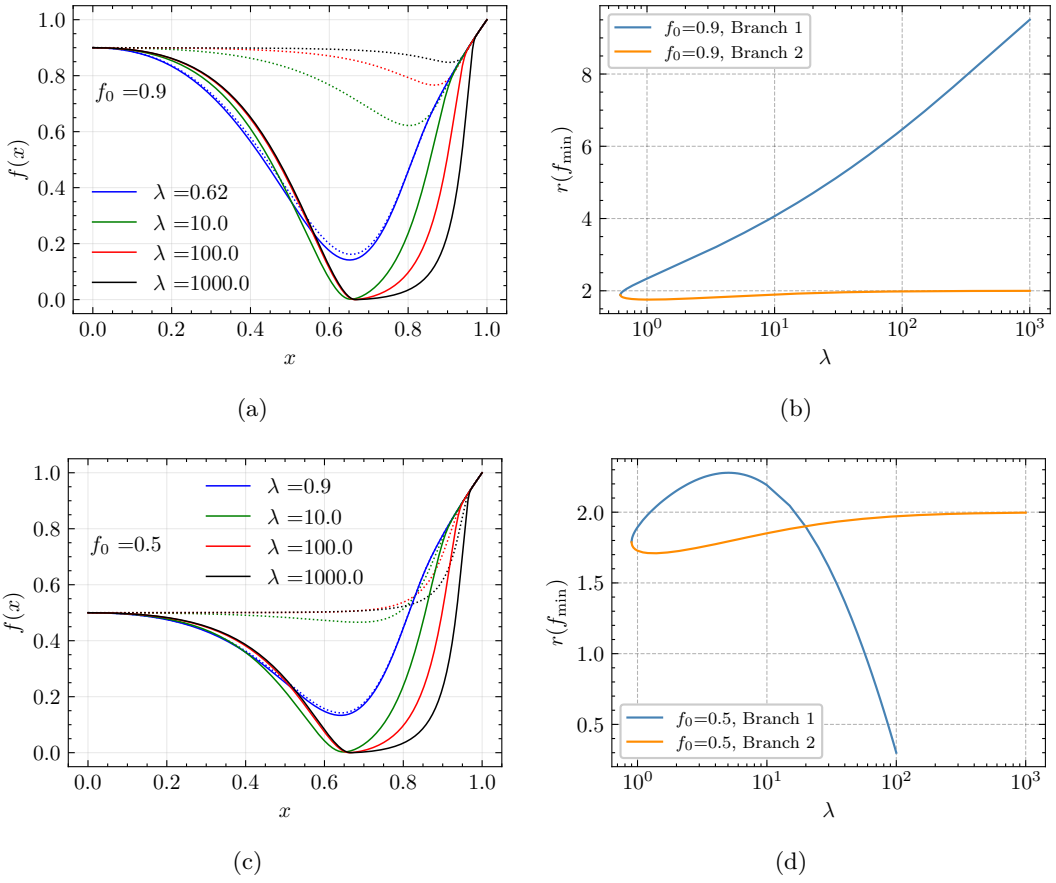


Figure 1. Solutions of $f(r)$ for (a) $f_0 = 0.9$ and (b) $f_0 = 0.5$. Curves with the same λ value correspond to the same color, where dashed and solid lines represent solutions in Branch 1 and Branch 2, respectively.

with

$$V(r) = \frac{1}{2} \frac{1}{g_{tt}g_{rr}} \left(E^2 + g_{tt} \left(1 + \frac{L^2}{g_{\phi\phi}} \right) \right) = -\frac{1}{2} E^2 + \frac{1}{2} f(r) \left(1 + \frac{L^2}{r^2} \right). \quad (3.6)$$

For a circular orbit (CO) satisfying $\dot{r} = 0$, we have $V(r_{\text{CO}}) = 0$, where r_{CO} denotes the radius of the circular orbit. To analyze its stability, the following effective potential is introduced:

$$V_{\text{eff}}(r) = \frac{1}{2} f(r) \left(1 + \frac{L^2}{r^2} \right). \quad (3.7)$$

When a massive particle moves in a circular orbit, its angular velocity is:

$$\Omega_{\text{CO}} = \frac{d\phi}{dt} = \frac{\dot{\phi}}{t} = \pm \sqrt{\frac{-\partial_r g_{tt}}{\partial_r g_{\phi\phi}}} = \pm \sqrt{\frac{f'(r)}{2r}}, \quad (3.8)$$

where the prime denotes the derivative with respect to r and $f'(r) \geq 0$.

Moreover, the specific angular momentum and the specific energy for a circular orbit are expressed as:

$$L_{\text{CO}} = \frac{g_{\varphi\varphi}\Omega_{\text{CO}}}{\sqrt{D(r)}}, \quad E_{\text{CO}} = -\frac{g_{tt}}{\sqrt{D(r)}}, \quad (3.9)$$

where function

$$D(r) = -g_{tt} - g_{\varphi\varphi}\Omega_{\text{CO}}^2 = \frac{2f(r) - rf'(r)}{2} \geq 0. \quad (3.10)$$

As shown in Fig. 2, we present the solutions of the function $D(r)$ in two branches with the parameter $f_0 = 0.9$. It can be observed that in Branch 2, when $\lambda > 1$, the minimum value of $D(r)$ is less than zero, which is distinctly different from the case in Branch 1. Since $D(r) < 0$ violates condition (3.10), the region allowing circular orbits becomes discontinuous. Moreover, when λ exceeds a certain critical value, the phenomenon where the minimum value of $D(r)$ is less than zero also appears in Branch 2 for other values of f_0 .

If we further consider the condition $f'(r) \geq 0$, the range allowing for the existence of circular orbits in Branch 2 will be further constrained. As shown in Fig. 3, we have marked the regions where $f'(r) < 0$ in red, the regions where $D(r) < 0$ in orange, and the regions that simultaneously satisfy $f'(r) \geq 0$ and $D(r) \geq 0$ (i.e., the regions where circular orbits are allowed) in green, with the parameters $f_0 = 0.9$ and $\lambda = 0.7$. It can be observed that, under the premise of satisfying all physical conditions ($f'(r) \geq 0$ and $D(r) \geq 0$), the region allowing for the existence of circular orbits is divided into two discontinuous parts.

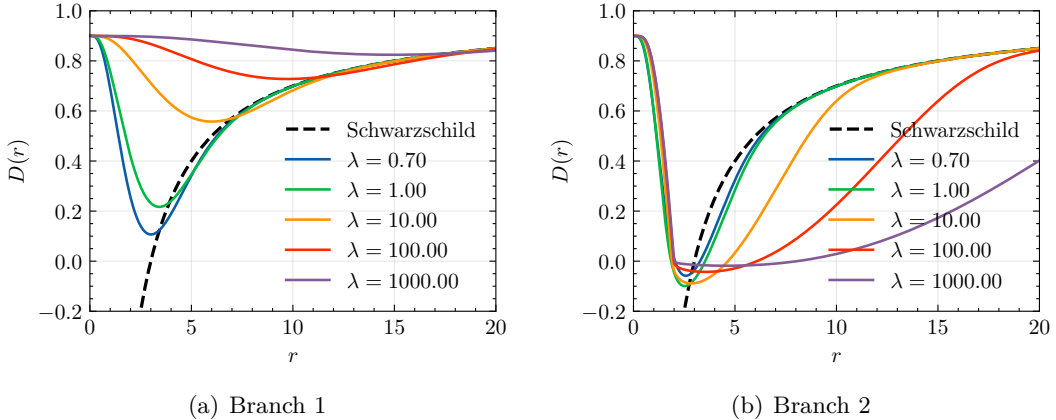


Figure 2. Plots of function $D(r)$ for different values of λ . The left panel (a) corresponds to Branch 1, while the right panel (b) corresponds to Branch 2. The dashed lines represent the Schwarzschild case, and the solid lines represent the ECG case with parameters $f_0 = 0.9$ and different values of λ .

The necessary conditions for stable circular orbits (SCOs) are:

$$V'_{\text{eff}}(r_{\text{SCO}}) = 0, \quad V''_{\text{eff}}(r_{\text{SCO}}) \geq 0, \quad (3.11)$$

where r_{SCO} denotes the radius of stable circular orbits and $V''_{\text{eff}}(r_{\text{SCO}}) = 0$ is the critical stability condition.

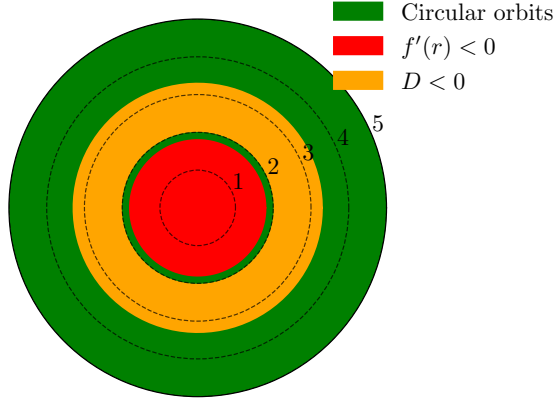


Figure 3. The region where circular orbits exist (green). The corresponding solution comes from Branch 2, with parameters $f_0 = 0.9$ and $\lambda = 0.7$. Here, $f'(r) < 0$ and $D(r) < 0$ are marked in red and orange, respectively, with the black dashed circle serving as a reference, and the numbers indicate its value of radius.

Let the radius of the static stable circular orbit be r_{SSCO} . On this orbit, the angular velocity of the particle satisfies $\Omega(r_{\text{SSCO}}) = 0$ (at the same time $L_{\text{CO}}(r_{\text{SSCO}}) = 0$), i.e.,

$$f'(r_{\text{SSCO}}) = 0. \quad (3.12)$$

Substituting $L_{\text{CO}}(r_{\text{SSCO}}) = 0$ and $f'(r_{\text{SSCO}}) = 0$ into equation (3.7), we can obtain

$$V'_{\text{eff}}(r_{\text{SSCO}}) = \frac{1}{2}f'(r_{\text{SSCO}}), \quad V''_{\text{eff}}(r_{\text{SSCO}}) = \frac{1}{2}f''(r_{\text{SSCO}}). \quad (3.13)$$

In summary, the conditions for the existence of a static stable timelike orbit can be stated as

$$f(r_{\text{SSCO}}) > 0, \quad f'(r_{\text{SSCO}}) = 0, \quad f''(r_{\text{SSCO}}) \geq 0. \quad (3.14)$$

As an example, Fig. 4 shows the effective potential energy $V_{\text{eff}}(r)$ and its first and second derivatives for particles with angular momentum $\Omega = 0$ in Branch 1, with parameters $f_0 = 0.9$ and $\lambda = 10$. The figure reveals that the effective potential energy has a minimum at $r = 4.065175$, where the conditions for a static stable orbit are satisfied: $V'_{\text{eff}}(r) = 0$ and $V''_{\text{eff}}(r) > 0$. Thus, the radius of the corresponding static stable circular orbit is determined to be $r_{\text{SSCO}} = 4.065175$. Further substituting this radius into the condition $V(r_{\text{SSCO}}) = 0$ yields the corresponding specific energy as $E = 0.788572$.

Next, we numerically integrate the geodesic equations (3.2)–(3.3) to visually verify the stability of the aforementioned orbit. The verification is conducted in two steps.

First, we test the stability of the orbit under angular velocity perturbations. As shown in Fig. 5, we fix the initial orbital radius of the particle at r_{SSCO} with zero radial velocity and apply angular velocity perturbations (initial angular velocities are $\Omega_0 = 0.01, 0.005$, and 0.0005 , respectively). The dashed line represents the static stable circular orbit, with an evolution over 300 proper time units. The results indicate: (1) As shown in Fig. 5a, all particles remain in motion near the static stable circular orbit; (2) As shown in Fig.

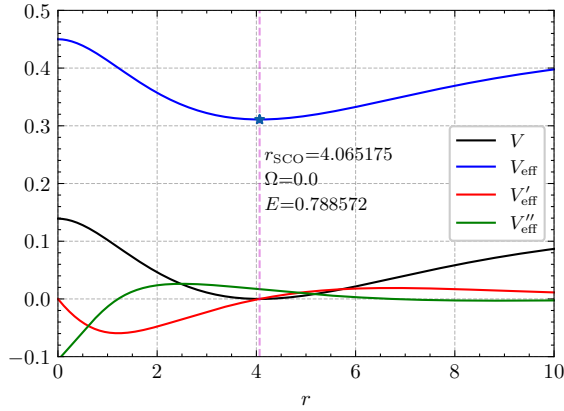


Figure 4. Effective potential for particles with zero angular velocity $\Omega = 0$. The corresponding solution come from Branch 1, with parameters $f_0 = 0.9$ and $\lambda = 10$. The blue star (\star) marks the location of the minimum of the effective potential. The vertical red dashed line indicates the location of the minimum of effective potential.

5b, the amplitude of orbital deviation gradually decreases as the initial angular velocity decreases.

Second, we test the stability of the orbit under radial perturbations. As depicted in Fig. 6, we fix the initial angular velocity at $\Omega_0 = 0.01$ with zero radial velocity and set initial radii of $r_0 = 3.9$ and $r_0 = 4.2$ as radial perturbations, evolving again over 300 proper time units. Fig. 6a reveals that the particles undergo bounded oscillations around the static stable circular orbit, with radial deviations shown in Fig. 6 b, where the maximum deviation remains constant.

Combining the results from Figs. 5 and 6, it is evident that whether perturbations are applied to the angular velocity or the radial position, the particle's trajectory remains confined near the static stable circular orbit. This confirms that the orbit with radius r_{SSCO} indeed corresponds to the static stable orbit for massive particles.

Moreover, when $r < r_{\text{SSCO}}$, $f'(r) < 0$, which is forbidden. Therefore, r_{SSCO} represents the innermost stable circular orbit (ISCO) permitted, i.e.,

$$r_{\text{ISCO}} = r_{\text{SSCO}}. \quad (3.15)$$

4 Aschenbach effect

In a spherically symmetric static spacetime, the orbital velocity $v^{(\phi)}$ of a massive particle moving along a circular orbit, as measured by a ZAMO observer, can be derived by simplifying the corresponding expression in Kerr spacetime [11, 46]:

$$v^{(\phi)} = \sqrt{\frac{-r g_{tt,r}}{2g_{tt}^2}} = \frac{\sqrt{rf'(r)/2}}{f(r)}.$$

In the Schwarzschild case, the orbital velocity $v^{(\phi)}$ monotonically increases as r decreases. For cubic gravity, in regions far from the center, its behavior resembles the

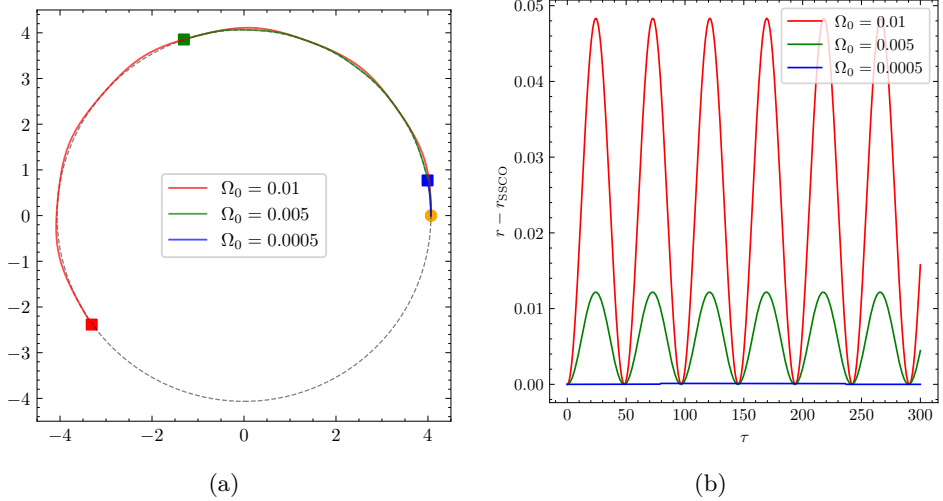


Figure 5. (a) The particle trajectory diagram, where the dashed reference circle has a radius of 4.065175, the solid orange circle represents the starting position, the solid square represents the ending position. The initial conditions are: radial coordinate $r_0 = 4.065175$, angular velocity Ω_0 , and zero radial velocity. (b) The radial deviation as a function of proper time. The solution is from Branch 1, with parameters $f_0 = 0.9$ and $\lambda = 10.0$.

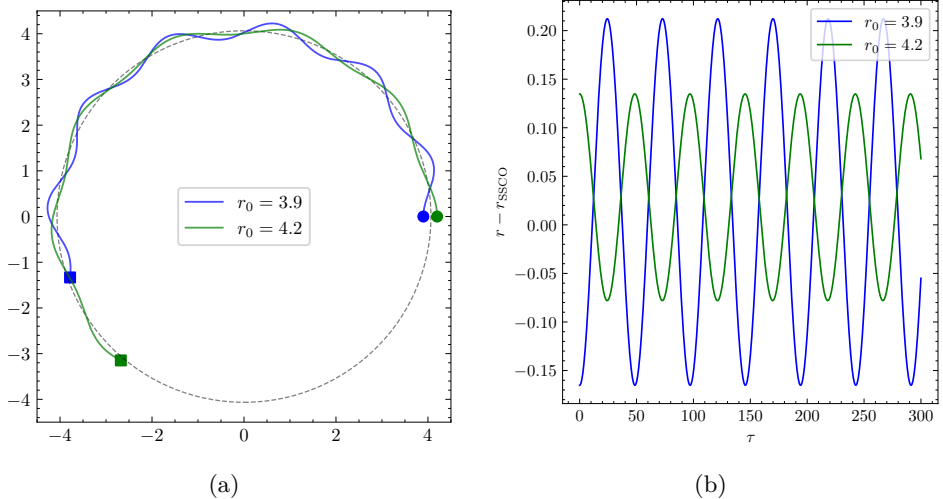


Figure 6. (a) The particle trajectory diagram, the dashed reference circular has radius 4.065175, the solid orange circle represents the starting position, the solid square represents the ending position. The initial conditions are: radial coordinate r_0 , angular velocity $\Omega_0 = 0.01$, and zero radial velocity. (b) The radial deviation as a function of proper time. The solution is from Branch 1, with parameters $f_0 = 0.9$ and $\lambda = 10.0$.

Schwarzschild solution, meaning $v^{(\phi)}$ increases as r decreases. However, near the gravitational center, $v^{(\phi)}$ decreases as r diminishes, exhibiting the typical Aschenbach effect, as shown in Figs. 7a and 7c. At the same time, Figs. 7b and 7d show that the variation of the circular orbital angular velocity Ω_{CO} with r is completely consistent with the

variation of $v^{(\phi)}$. This further supports the view of point that in a spherically symmetric static spacetime, the non-monotonic behavior of orbital angular velocity with respect to the radial coordinate can serve as an effective criterion for the Aschenbach effect [8–10].

In Branch 2, for larger values of λ , the presence of regions with $f'(r) < 0$ and $D(r) < 0$ (as shown in Fig. 3) leads to discontinuities in the curves of $v^{(\phi)}$ and Ω_{CO} , as illustrated in Figs. 7c and 7d.

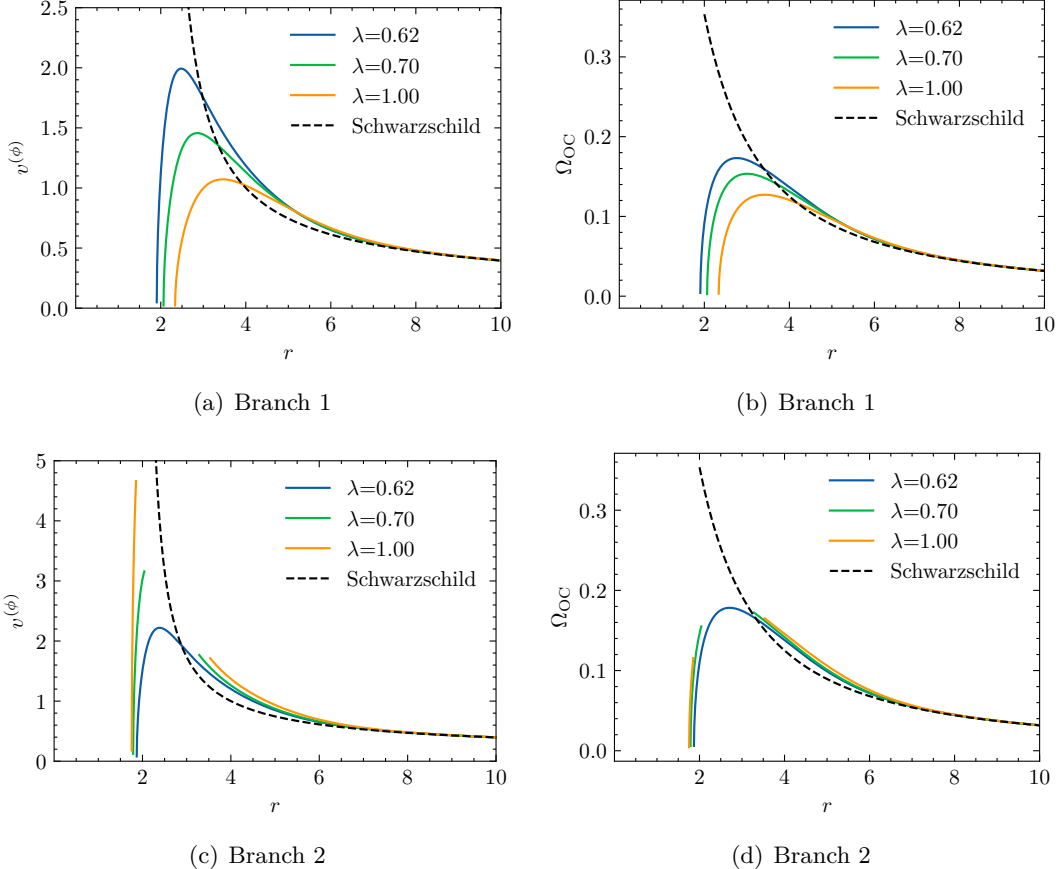


Figure 7. The distribution of the orbital velocity $v^{(\phi)}$ of massive particles relative to ZAMO, and the distribution of the angular velocity Ω_{CO} of massive particles relative to a distant observer. The first row corresponds to Branch 1, and the second row corresponds to Branch 2, with the parameter $f_0 = 0.9$. The dashed line represent the Schwarzschild solution.

Except for $v^{(\phi)}$ and Ω_{CO} , the specific energy E of a massive particle on a circular orbit also exhibits a non-monotonic variation with the orbital radius, as shown in Fig. 8. Here, Fig. 8a shows the case of Branch 1, where E remains finite across the entire region. However, for the case of Branch 2 depicted in Fig. 8c, E diverges at certain locations, similar to the case of a Schwarzschild black hole, where the divergence points correspond to the position of the photon sphere.

The effective potential of photons:

$$V_{\text{eff,photon}}(r) = \frac{f(r)}{r^2}, \quad (4.1)$$

where the photon sphere radius is determined by

$$V'_{\text{eff,photon}}(r) = \frac{rf'(r) - 2f(r)}{r^3} = -\frac{2D(r)}{r^3} = 0, \quad (4.2)$$

i.e., the location where $D(r) = 0$. As indicated by Eq. (3.9), the specific energy E of the particle tends to diverge at this position.

Furthermore, Figs. 8b and 8d show the distribution of the E on stable circular orbits. It can be observed that orbits near the gravitational center can also remain stable. It is noteworthy that for massive particles in stable circular orbits near the gravitational center, their specific energy E also decreases as the orbital radius decreases, and when the orbital radius is large, E is generally greater than 1. This means that when these massive particles on the nearly central stable orbits lose energy, they can smoothly transition to orbits with smaller radii and lower energy, while releasing energy exceeding their rest mass in this process (for Branch 1, this requires a larger λ). Similar stable orbits also exist in the model discussed in Ref. [8]. The difference is that their model describes a black hole solution, in which the orbits closer to the gravitational center are unstable ones.

5 Conclusions and discussions

Within the framework of Einsteinian Cubic Gravity (ECG), we investigated the structure of timelike geodesics around a class of static, spherically symmetric, horizonless compact objects. The study revealed that in such purely gravitational, electrically neutral spacetimes, there exist static stable circular orbits. These orbits not only allow test particles to remain static relative to an observer at infinity but also correspond to the innermost stable circular orbit (ISCO) within this spacetime. If such orbits form part of an accretion disk, their optical images would exhibit a ring which unaffected by Doppler shifts, providing a potential distinguishing feature for differentiating ECG horizonless compact objects from Schwarzschild black holes through astronomical observations.

Through numerical analysis, we found that at larger radii, where the spacetime resembles the Schwarzschild solution, the angular velocity Ω_{CO} and orbital velocity $v^{(\phi)}$ monotonically increase as the radius decreases. However, as the orbit approaches the gravitational center, both velocities exhibit non-monotonic behavior—first increasing and then decreasing until they drop to zero at the static orbit, which is a typical manifestation of the Aschenbach effect. This effect has been observed in both branches of the ECG solution. Additionally, in Branch 2, when the coupling parameter λ is large, the distribution region of circular orbits becomes discontinuous due to the emergence of regions where $D(r) < 0$ and $f'(r) < 0$.

Furthermore, our analysis of the specific energy of particles shows that, across most parameter ranges (for large λ in Branch 1), stable circular orbits near the gravitational center exhibit $E > 1$. This means that when particles lose energy and transition from these orbits ($E > 1$) to the static stable circular orbits, they can release energy exceeding their rest mass.

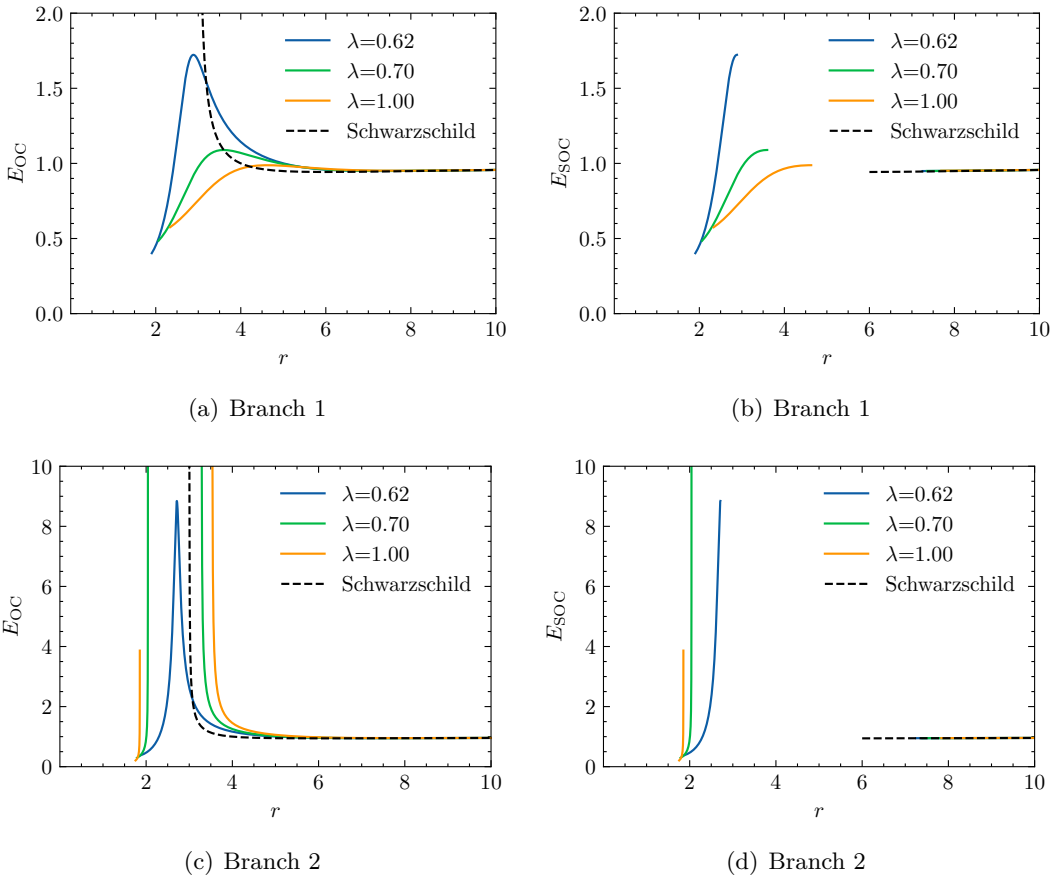


Figure 8. The distribution of specific energy E of massive particles on circular orbits (the first column) and the stable circular orbits (the second column). The first and second rows correspond to Branch 1 and Branch 2 respectively, with parameter values of $f_0 = 0.9$. The dashed line represent the Schwarzschild solution.

In our future work, we plan to study the radiation model of the accretion disk around ECG horizonless objects and explore the optical characteristics of accretion disks that include static orbital rings.

6 Acknowledgment

This work is supported by the National Natural Science Foundation of China (Grant No.12275110 and No. 12247101) and the National Key Research and Development Program of China (Grant No. 2022YFC2204101 and 2020YFC2201503).

References

- [1] LIGO SCIENTIFIC, VIRGO collaboration, B. Abbott, R. Abbott, T. Abbott et al., *Observation of Gravitational Waves from a Binary Black Hole Merger*, *Phys. Rev. Lett.* **116** (2016) 061102 [[1602.03837](https://arxiv.org/abs/1602.03837)].

[2] EVENT HORIZON TELESCOPE collaboration, K. Akiyama, A. Alberdi, W. Alef et al., *First M87 Event Horizon Telescope Results. I. The Shadow of the Supermassive Black Hole*, *Astrophys. J. Lett.* **875** (2019) L1 [[1906.11238](#)].

[3] EVENT HORIZON TELESCOPE collaboration, K. Akiyama, A. Alberdi, W. Alef et al., *First Sagittarius A* Event Horizon Telescope Results. I. The Shadow of the Supermassive Black Hole in the Center of the Milky Way*, *Astrophys. J. Lett.* **930** (2022) L12 [[2311.08680](#)].

[4] L. G. Collodel, B. Kleihaus and J. Kunz, *Static Orbits in Rotating Spacetimes*, *Phys. Rev. Lett.* **120** (2018) 201103 [[1711.05191](#)].

[5] M. C. Teodoro, L. G. Collodel and J. Kunz, *Retrograde Polish Doughnuts around Boson Stars*, *JCAP* **03** (2021) 063 [[2011.10288](#)].

[6] M. C. Teodoro, L. G. Collodel, D. Doneva, J. Kunz, P. Nedkova and S. Yazadjiev, *Thick toroidal configurations around scalarized Kerr black holes*, *Phys. Rev. D* **104** (2021) 124047 [[2108.08640](#)].

[7] S.-W. Wei, Y.-P. Zhang, Y.-X. Liu and R. B. Mann, *Static spheres around spherically symmetric black hole spacetime*, *Phys. Rev. Res.* **5** (2023) 043050 [[2303.06814](#)].

[8] P. K. Yerra, S. Mukherji and C. Bhamidipati, *Static spheres and Aschenbach effect for black holes in massive gravity*, *Phys. Rev. D* **111** (2025) 124018 [[2411.01261](#)].

[9] S.-W. Wei and Y.-X. Liu, *Aschenbach effect and circular orbits in static and spherically symmetric black hole backgrounds*, *Phys. Dark Univ.* **43** (2023) 101409 [[2308.11883](#)].

[10] M. A. S. Afshar and J. Sadeghi, *Mechanisms behind the aschenbach effect in non-rotating black hole spacetime*, *Ann. Phys.* **474** (2025) 169953 [[2412.06357](#)].

[11] B. Aschenbach, *Measuring mass and angular momentum of black holes with high-frequency quasi-periodic oscillations*, *Astron. Astrophys.* **425** (2004) 1075 [[astro-ph/0406545](#)].

[12] B. Aschenbach, *Mass and angular momentum of Sgr A**, in *Conference on Growing Black Holes: Accretion in a Cosmological Context*, Oct., 2004, [astro-ph/0410328](#), DOI.

[13] B. Aschenbach, *Mass and Angular Momentum of Black Holes: An Overlooked Effect of General Relativity Applied to the Galactic Center Black Hole Sgr A**, *Chin. J. Astron. Astrophys.* **6** (2006) 1221 [[astro-ph/0603193](#)].

[14] Z. Stuchlík, P. Slaný, G. Török and M. A. Abramowicz, *Aschenbach effect: Unexpected topology changes in the motion of particles and fluids orbiting rapidly rotating kerr black holes*, *Phys. Rev. D* **71** (2005) 24037 [[gr-qc/0411091](#)].

[15] A. Mueller and B. Aschenbach, *Non-monotonic orbital velocity profiles around rapidly rotating kerr-(anti-)de sitter black holes*, *Cl., Quant., Grav.* **24** (2007) 2637 [[0704.3963](#)].

[16] Z. Stuchlik, M. Blaschke and P. Slany, *Non-monotonic keplerian velocity profiles around near-extreme braneworld kerr black holes*, *Cl., Quant., Grav.* **28** (2011) 175002 [[1108.0191](#)].

[17] A. Tursunov, Z. Stuchlík and M. Kološ, *Circular orbits and related quasiharmonic oscillatory motion of charged particles around weakly magnetized rotating black holes*, *Phys. Rev. D* **93** (2016) 084012 [[1603.07264](#)].

[18] J. Khodagholidzadeh, V. Perlick and A. Vahedi, *Aschenbach effect for spinning particles in kerr spacetime*, *Phys. Rev. D* **102** (2020) 24021 [[2002.04701](#)].

[19] A. Vahedi, J. Khodagholidzadeh and A. Tursunov, *Aschenbach effect for spinning particles in kerr-(a)dS spacetime*, *Eur. Phys. J. C* **81** (2021) 280 [[2103.14912](#)].

[20] Y.-Q. Wang, *Frozen gravitational stars in Einsteinian cubic gravity*, *arXiv:2410.04575 [gr-qc]* (2024) [[2410.04575](#)].

[21] P. Bueno and P. A. Cano, *Einsteinian cubic gravity*, *Phys. Rev. D* **94** (2016) 104005 [[1607.06463](#)].

[22] P. Bueno and P. A. Cano, *Four-dimensional black holes in Einsteinian cubic gravity*, *Phys. Rev. D* **94** (2016) 124051 [[1610.08019](#)].

[23] R. A. Hennigar and R. B. Mann, *Black holes in Einsteinian cubic gravity*, *Phys. Rev. D* **95** (2017) 064055 [[1610.06675](#)].

[24] D. J. Burger, W. T. Emond and N. Moynihan, *Rotating black holes in cubic gravity*, *Phys. Rev. D* **101** (2020) 084009 [[1910.11618](#)].

[25] C. Adair, P. Bueno, P. A. Cano, R. A. Hennigar and R. B. Mann, *Slowly rotating black holes in Einsteinian cubic gravity*, *Phys. Rev. D* **102** (2020) 084001 [[2004.09598](#)].

[26] P. A. Cano and D. Pereñiguez, *Extremal rotating black holes in einsteinian cubic gravity*, *Phys. Rev. D* **101** (2020) 044016 [[1910.10721](#)].

[27] A. M. Frassino and J. V. Rocha, *Charged black holes in einsteinian cubic gravity and nonuniqueness*, *Phys. Rev. D* **102** (2020) 024035 [[2002.04071](#)].

[28] M. Kord Zangeneh and A. Kazemi, *Topological born–infeld charged black holes in einsteinian cubic gravity*, *Eur. Phys. J. C* **80** (2020) 794 [[2003.04458](#)].

[29] S. N. Sajadi and S. H. Hendi, *Analytically approximation solution to einstein-cubic gravity*, *Eur. Phys. J. C* **82** (2022) 675 [[2207.13435](#)].

[30] L. A. Lessa and J. E. G. Silva, *Regular black holes in einstein cubic gravity*, *arXiv:2305.18254 [gr-qc]* (2023) [[2305.18254](#)].

[31] H. R. Bakhtiarizadeh, *Charged rotating black strings in einsteinian cubic gravity*, *Phys. Rev. D* **105** (2022) 064037 [[2111.02663](#)].

[32] H. R. Bakhtiarizadeh and H. Golchin, *Rotating black strings in einsteinian cubic gravity with born–infeld electrodynamics*, *Iran. J. Phys. Res.* **22** (2022) 663.

[33] P. Bueno, P. A. Cano, J. Moreno and Á. Murcia, *All higher-curvature gravities as Generalized quasi-topological gravities*, *JHEP* **11** (2019) 062 [[1906.00987](#)].

[34] A. Cisterna, N. Grandi and J. Oliva, *On four-dimensional Einsteinian gravity, quasitopological gravity, cosmology and black holes*, *Phys. Lett. B* **805** (2020) 135435 [[1811.06523](#)].

[35] C. Erices, E. Papantonopoulos and E. N. Saridakis, *Cosmology in cubic and $f(P)$ gravity*, *Phys. Rev. D* **99** (2019) 123527 [[1903.11128](#)].

[36] I. Quiros, R. García-Salcedo, T. Gonzalez, J. L. M. Martínez and U. Nucamendi, *Global asymptotic dynamics of cosmological einsteinian cubic gravity*, *Phys. Rev. D* **102** (2020) 044018 [[2003.10516](#)].

[37] S. Dengiz, *Cosmological weyl-einsteinian-cubic gravity as a gauge theory of gravity*, *Eur. Phys. J. C* **85** (2025) 928 [[2408.04282](#)].

[38] M. R. Mehdizadeh and A. H. Ziaie, *Traversable wormholes in einsteinian cubic gravity*, *Mod. Phys. Lett. A* **35** (2019) 2050017 [[1903.10907](#)].

- [39] I. Hussain and G. Mustafa, *Traversable wormholes in einsteinian-cubic-gravity with hybrid shape functions*, *Int. J. Geom. Meth. Mod. Phys.* **19** (2022) 2250074.
- [40] G. Mustafa, T.-C. Xia, I. Hussain and M. F. Shamir, *Spherically symmetric static wormhole models in the einsteinian cubic gravity*, *Int. J. Geom. Meth. Mod. Phys.* **17** (2020) 2050214.
- [41] G. Mustafa, F. Atamurotov and S. G. Ghosh, *Structural properties of generalized embedded wormhole solutions via dark matter halos in einsteinian-cubic-gravity with quasi-periodic oscillations*, *Phys. Dark Univ.* **40** (2023) 101214.
- [42] M. Lu, J. Yang and R. B. Mann, *Existence of vacuum wormholes in Einsteinian cubic gravity*, *JHEP* **3** (2025) 73 [[2410.13996](#)].
- [43] M. S. Alnaes, A. Logg, K. B. Ølgaard, M. E. Rognes and G. N. Wells, *Unified Form Language: A domain-specific language for weak formulations of partial differential equations*, *ACM Transactions on Mathematical Software* **40** (2014) .
- [44] M. W. Scroggs, I. A. Baratta, C. N. Richardson and G. N. Wells, *Basix: A runtime finite element basis evaluation library*, *Journal of Open Source Software* **7** (2022) 3982.
- [45] I. A. Baratta, J. P. Dean, J. S. Dokken, M. Habera, J. S. Hale, C. N. Richardson et al., *DOLFINx: The next generation FEniCS problem solving environment*, Dec., 2023. 10.5281/zenodo.10447666.
- [46] A. Mueller and M. Camenzind, *Relativistic emission lines from accreting black holes - The effect of disk truncation on line profiles*, *Astron. Astrophys.* **413** (2004) 861 [[astro-ph/0309832](#)].